

# Ultra-low glassy thermal conductivity and controllable, promising thermoelectric properties in crystalline $o\text{-CsCu}_5\text{S}_3$

Jincheng Yue<sup>#,a</sup>, Jiongzhi Zheng<sup>#,\*,b,c</sup>, Junda Li<sup>a</sup>, Siqi Guo<sup>a</sup>, Wenling Ren<sup>d</sup>, Han Liu<sup>e</sup>, Yanhui Liu<sup>†a</sup> and Tian Cui<sup>‡a,f</sup>

<sup>a</sup>*Institute of High Pressure Physics, School of Physical Science and Technology, Ningbo University, Ningbo 315211, China.*

<sup>b</sup>*Thayer School of Engineering, Dartmouth College, Hanover, New Hampshire, 03755, USA.*

<sup>c</sup>*Department of Mechanical and Aerospace Engineering, The Hong Kong University of Science and Technology, Clear Water Bay, Kowloon, Hong Kong.*

<sup>d</sup>*Institute of Materials Science, Technical University of Darmstadt, Alarich-Weiss-Strasse 2, 64287 Darmstadt, Germany.*

<sup>e</sup>*School of Control Science and Engineering, Dalian University of Technology, Dalian 116024, China.*

<sup>f</sup>*State Key Laboratory of Superhard Materials, College of Physics, Jilin University, Changchun 130012, China.*

January 31, 2024

---

<sup>0</sup># these authors contributed equally.

\*Corresponding author:Email:jiongzhi.zheng@dartmouth.edu

†Corresponding author:Email:liuyanhui@nbu.edu.cn

‡Corresponding author:Email:cuitian@nbu.edu.cn

## 1 ABSTRACT

Fundamental understanding of anharmonic lattice dynamics and heat conductance physics in crystalline materials is crucial for the development of energy conversion devices. Here, we thoroughly investigate the microscopic mechanisms of the thermal transport in orthorhombic  $o$ -CsCu<sub>5</sub>S<sub>3</sub> by integrating the first-principles-based self-consistent phonon calculations (SCP) with the linearized Wigner transport equation (LWTE). Our methodology takes into account contributions to phonon energy shifts and phonon scattering rates from both three- and four-phonon processes. Additionally, it incorporates the off-diagonal terms of heat flux operators to calculate the total thermal conductivity. The predicted  $\kappa_{\perp}$  with an extremely weak temperature dependence following  $\sim T^{-0.33}$ , in good agreement with experimental values along with the parallel to the Bridgman growth direction. Such nonstandard temperature dependence of  $\kappa_{\perp}$  can be traced back to the dual particlelike-wavelike behavior exhibited by thermal phonons. Specifically, the coexistence of the stochastic oscillation of Cs atoms and metavalent bonding among interlayer Cu-S atoms limits the particle-like phonon propagation and enhances the wave-like tunneling of phonons. Simultaneously, the electrical transport properties are determined by employing a precise momentum relaxation-time approximation (MRTA) within the framework of the linearized Boltzmann transport equation (LBTE). By properly adjusting the carrier concentration, excellent thermoelectric performance is achieved, with a maximum thermoelectric conversion efficiency of 18.4% observed at 800 K in  $p$ -type  $o$ -CsCu<sub>5</sub>S<sub>3</sub>. Our work not only elucidates the anomalous thermal transport behavior in the copper-based chalcogenide  $o$ -CsCu<sub>5</sub>S<sub>3</sub> but also provides insights for manipulating its thermal and electronic properties for potential thermoelectric applications.

## 2 INTRODUCTION

Thermoelectric materials, directly converting heat into electricity, are presently being explored for various feasible waste heat recovery systems, including space-based applications and thermal data storage devices [1, 2, 3, 4]. Generally, the thermoelectric maximum efficiency of thermoelectric materials is characterized by the dimensionless figure of merit [5, 6, 7],  $ZT = S^2\sigma/\kappa$ , where  $S$ ,  $\sigma$ , and  $\kappa$  represent the Seebeck coefficient, electrical conductivity, and thermal conductivity, respectively. A central focus in thermoelectric materials research is to notably

enhance conversion efficiency by minimizing irreversible heat transport and preserving favorable electrical transport properties [8, 9, 10, 11]. Thus, the proposal of the phonon glass electron-crystal (PGEC) concept aims to identify high-performance thermoelectric materials [12, 13]. In this paradigm, ordered crystals preserve favorable electronic properties while demonstrating lattice thermal conductivity ( $\kappa_L$ ) comparable to amorphous solids or glasses. Nonetheless, the pursuit of a net increase in the power factor poses a challenge to enhancing thermoelectric performance due to the strong coupling among electrical transport [14, 15]. Therefore, a comprehensive exploration of the microscopic mechanisms governing thermal transport in crystalline semiconductors is vital for optimizing and controlling high-performance thermoelectric devices.

To achieve low thermal conductivity in crystalline solids, various strategies have been proposed, including nanostructuring [16], atomic rattling [17, 18], strong lattice anharmonicity [19], and liquid-like ions [20]. For instance, the presence of rattlers results in a tenfold reduction in the phonon lifetime by enhancing the scattering phase space in clathrate  $\text{Ba}_8\text{Ga}_{16}\text{Ge}_{30}$  (BGG) [21]. While the strong anharmonic lattice vibration induced by the host-guest framework leads to significant anharmonic phonon scattering, this cage also facilitates electrical transport through a smooth channel and constitutes a PGEC system. In addition, superionic conductors (SICs), e.g.,  $\text{Cu}_2\text{Se}_{1-x}\text{S}_x$  [22, 23],  $\text{KAg}_3\text{Se}_2$  [24, 25], and  $\text{AgCrSe}_2$  [26], exhibit ultra-low  $\kappa_L$  of  $< 1 \text{ Wm}^{-1}\text{K}^{-1}$  attributed to their part-crystalline part-liquid nature. Specifically, the liquid-like ionic diffusion suppresses the transverse acoustic phonons, resulting in a reduction in heat capacity and heat conductance [27]. Moreover, the disordered arrangement of atoms induced by the liquid-like sublattice enhances the scattering rates of main heat carriers, i.e., longitudinal acoustic modes, further contributing to the reduction in thermal conductivity [26, 28]. In contrast, single crystals with regular atomic arrangement and ultra-low  $\kappa_L$  have rarely been investigated in depth.

Copper-based chalcogenides have recently demonstrated advantages over traditional thermoelectric materials in industrial applications, primarily due to their nontoxicity, low cost, and environmental benignity [29, 30]. Among them,  $\text{Cu}_{1.97}\text{S}$  stands out, demonstrating high thermoelectric performance with a ZT value of 1.7 at 1000 K,

achieved through appropriate copper deficiency [30]. Nevertheless, the reliability of these devices faces challenges due to deformations resulting from multiple phase transitions and the liquid-like migration of constituent elements. Previously inspired by the synthesis of layered  $o\text{-CsCu}_5\text{S}_3$  for photovoltaic applications [31, 32], its intrinsically ultra-low  $\kappa_L$  of  $< 0.6 \text{ Wm}^{-1}\text{K}^{-1}$  and high phase transition temperature of 823 K have significantly advanced its role in the realm of thermoelectricity [33]. Moreover, the experiment unveils the complete localization of all Cu atoms in  $o\text{-CsCu}_5\text{S}_3$  on their designated Wyckoff sites with full occupancy. This strategic localization emerges as an effective preventive measure against device degradation. Moreover,  $o\text{-CsCu}_5\text{S}_3$  displays a nonstandard glass-like temperature dependence—a rare characteristic in crystalline materials without impurities, disorder, and complex configurations. Nevertheless, fundamental research on its thermal conductivity is still lacking despite its practical significance.

In this work, we thoroughly investigate the thermal and electrical transport properties in crystalline  $o\text{-CsCu}_5\text{S}_3$  at the atomic level using first-principles density functional theory. Specifically, we integrate the state-of-the-art linearized Wigner transport equation (LWTE) and self-consistent phonon (SCP) theory to elucidate the thermal transport mechanisms in  $o\text{-CsCu}_5\text{S}_3$ . By accounting for contributions to phonon energies and scattering rates from both cubic and quartic anharmonicities, we can well reproduce the experimental thermal conductivity and its temperature dependence. Meanwhile, the electrical transport properties are characterized by employing an accurate momentum relaxation-time approximation (MRTA) within the framework of the linearized Boltzmann transport equation (LBTE). Upon optimally tuning the carrier concentration, the theoretical maximum thermoelectric performance can achieve 18.4% at 800 K, indicating its potential to meet critical criteria for thermoelectric materials. Our work elucidates the microscopic mechanisms behind the anomalous thermal conductivity in crystalline  $o\text{-CsCu}_5\text{S}_3$  and evaluates its practical application as a promising thermoelectric device.

### 3 Methods

In this study, all density functional theory (DFT) calculations were carried out using the Vienna ab initio Simulation Package (VASP) [34, 35]. The project augmented wave (PAW) pseudopotentials were used to treat the Cs( $5s^25p^66s^1$ ), Cu( $3d^{10}4s^1$ ) and S( $3s^23p^4$ ) shells as valence

states [36]. The Perdew-Burke-Ernzerhof functional (PBE) within the generalized gradient approximation (GGA) was employed for the exchange-correlation functional [37], and the optB86b-vdW was used to accurately describe the van der Waals (vdW) interactions [38]. A kinetic energy cutoff value of 600 eV and a  $20 \times 20 \times 12$  Monkhorst-Pack electronic  $k$ -point grid were adopted to sample the Brillouin zone for the primitive cell. Tight energy and force convergence criteria of  $10^{-8}$  eV and  $10^{-6}$  eV $\cdot\text{\AA}^{-1}$ , respectively, were employed for both structural optimization and self-consistent DFT calculations.

The zero-K harmonic ( $2^{nd}$ -order) force constants (IFCs) were extracted using the finite-displacement approach [39]. Static DFT calculations were performed using a  $3 \times 2 \times 2$  supercell containing 216 atoms, and a  $4 \times 4 \times 4$   $k$ -point meshes. To efficiently extract higher-order anharmonic IFCs, we constructed a displacement-force dataset with 200 atomic structures. Uniform displacements of 0.15  $\text{\AA}$  were enforced on all atoms along random directions using the random-seed method for reducing the cross-correlations between the atomic structures. The compressive sensing lattice dynamics (CSLD) approach [40, 41, 42] and the least absolute shrinkage and selection operator (LASSO) technique [43], implemented in the ALAMODE package [44, 45], were employed to screen the physically important terms of IFCs.

After obtaining the harmonic and anharmonic IFCs, the anharmonic phonon energy renormalization was carried out by applying the self-consistent phonon theory in the reciprocal space [46, 21]. Assuming only the first-order perturbation due to the quartic anharmonicity, namely the loop diagram, and ignoring the polarization mixing (PM) [44], the SCP equation can be derived in the diagonal form as follows:

$$\Omega_q^2 = \omega_q^2 + 2\Omega_q I_q \quad (1)$$

$$I_q = \frac{1}{8N} \sum_{q'} \frac{\hbar V^{(4)}(q; -q; q'; -q')}{4\Omega_q^2 \Omega_{q'}^2} [1 + 2n(\Omega_{q'})] \quad (2)$$

where  $\omega_q^2$  is the bare harmonic phonon frequency associated with the phonon mode  $q$ , and  $\Omega_q^2$  is the anharmonically renormalized phonon frequency at finite temperatures. The  $n$  and  $V^{(4)}(q; -q; q'; -q')$  represent the Bose-Einstein distribution ( $n(\omega) = 1/[\exp(\hbar\omega/k_B T) - 1]$ ), and the reciprocal representation of 4th-order IFCs, respectively. Within the framework of quasi-particle (QP) approximation and utilizing phonon

energies renormalized by loop diagram, the additional negative frequency shifts ascribing from the bubble self-energy can be estimated by the following self-consistent equation[21, 47]

$$(\Omega_q^B)^2 = \Omega_q^2 - 2\Omega_q \text{Re} \sum_B^q [G, \Phi_3](\Omega = \Omega_q^B) \quad (3)$$

where  $\sum_B^q [G, \Phi_3]$ ,  $B$ , and  $\Phi_3$  denote the frequency-dependent bubble self-energy, bubble diagram, and third-order force constant, respectively. Noteworthily, the QP-NL treatment option [48] was chosen to solve Eq. (3) and obtain the fully renormalized phonon energies that account for cubic and quartic anharmonicities.

Within the linearized Wigner transport equation (LWTE) framework [49, 50], the thermal conductivity  $\kappa_L^{\text{P/C}}$  can be described as

$$\begin{aligned} \kappa_L^{\text{P/C}} &= \frac{\hbar^2}{k_B T^2 V N_0} \sum_q \sum_{j,j'} \frac{\Omega_{qj} + \Omega_{qj'}}{2} v_{qjj'} \otimes v_{qjj'} \\ &\times \frac{\Omega_{qj} n_{qj} (n_{qj} + 1) + \Omega_{qj'} n_{qj'} (n_{qj'} + 1)}{4(\Omega_{qj} - \Omega_{qj'})^2 + (\Gamma_{qj} + \Gamma_{qj'})^2} (\Gamma_{qj} + \Gamma_{qj'}) \end{aligned} \quad (4)$$

where the  $V$  and  $N_0$  denote the primitive-cell volume and number of sampled, respectively. The  $\Gamma_q$  stands for the scattering rates including three-phonon (3ph), four-phonon (4ph), and isotope-phonon scattering processes [47, 51, 52]. The phonon group velocity  $v_q$  is extended to encompass off-diagonal components [53].

$$v_{qj'j} = \frac{\left\langle e_{qj} \left| \frac{\partial D(q)}{\partial q} \right| e_{qj'} \right\rangle}{2\sqrt{\Omega_{qj}\Omega_{qj'}}} \quad (5)$$

in which the  $D(q)$  and  $e_q$  are the dynamical matrix and polarization vector, respectively. The particle-like phonon thermal transport properties are computed by using the ShengBTE [54] and FourPhonon packages [55], while the wave-like tunneling of phonon channels is evaluated using our in-house code.

The related electronic transport was performed using the AMSET code [56] where the transition rates of electrons from the initial  $\psi_{nk}$  to final states  $\psi_{mk+q}$  based on Fermi's golden rule, which can be described as

$$\tilde{\tau}_{nk \rightarrow mk+q}^{-1} = \frac{2\pi}{\hbar} |g_{nm}(k, q)|^2 \delta(\epsilon_{nk} - \epsilon_{mk+q}) \quad (6)$$

where  $\epsilon_{nk}$  symbolizes the specific energy state  $\psi_{nk}$ . The  $g_{nm}(k, q)$  accounts for three kinds of electron-phonon scattering matrix elements including acoustic deformation potential (ADP) [57], polar optical phonon (POP) [58], and ionized impurity (IMP) [59] matrix element. The relaxation time of each electron can be evaluated by Matthiessen's rule, which is followed by

$$\tau_{nk}^{-1} = \tau_{ADP}^{-1} + \tau_{POP}^{-1} + \tau_{IMP}^{-1} \quad (7)$$

Moreover, the net atomic charges and the overlap populations were obtained by using the density-derived electrostatic and chemical (DDEC6) method in Chargemol [60, 61, 62]. Meanwhile, the Multiwfn 3.8 program [63] was employed to analyze the interactions by computing the interaction region indicators (IRI) [64], which can be described as  $IRI(\mathbf{r}) = |\nabla\rho(\mathbf{r})|/[\rho(\mathbf{r})]^a$  (Here the  $a$  is a tunable parameter, we adopt  $a=1.1$  for the standard definition of IRI). The correlative electronic wavefunction was achieved by Gaussian program [65], and visualization was realized in the VMD 1.9.3 program [66], where the BGR color scale was adopted.

## 4 Results and discussion

### 4.1 Configuration and bonding analysis

**Crystal structure and bonding strength.** The orthorhombic crystal structure of  $o\text{-CsCu}_5\text{S}_3$  is described by a space group of Pmma (No. 55) with computed lattice parameters  $a = 3.896 \text{ \AA}$ ,  $b = 8.857 \text{ \AA}$ , and  $c = 9.579 \text{ \AA}$ . Notably, these values are in good agreement with both experimental observations ( $a = 3.954 \text{ \AA}$ ,  $b = 8.949 \text{ \AA}$ , and  $c = 9.636 \text{ \AA}$ ) and other theoretical calculations [31, 67]. The  $o\text{-CsCu}_5\text{S}_3$  structures are derived from the  $\text{Cu}_4\text{S}_4$  columnar structural motif, which consists of the  $\text{Cu}_1$  and  $\text{Cu}_2$  atoms with three-fold coordination. [see Fig. S1] Specifically, these  $\text{Cu}_4\text{S}_4$  units propagate with periodicity along [001] directions and form a wavy layer by extending from two opposite sides through the  $\text{Cu}_3$  atom with a two-fold coordination [33]; meanwhile, an array of  $\text{Cs}^+$  cations is accommodated between them, as shown in Fig. 1(a).

The features of the structural configuration affect the interatomic force constants (IFCs) of the nearest-neighbor atom pairs and the distribution of electronic charge density, as shown in Fig.1(b). The IFC ( $|\Phi|$ ) for the Cu-S bond has the highest value of  $5.8 \text{ eV/\AA}^2$ , which

suggests a high degree of covalency between the Cu and S atoms. However, the Cs atoms interact weakly with the rest of the lattice in an ionic manner, which is evidenced by the small IFC values of the Cs-Cu ( $0.46 \text{ eV/\AA}^2$ ) and Cs-S ( $0.62 \text{ eV/\AA}^2$ ) pairs. As a result, the Cs atom will be positioned in a deeper potential well than the Cu and S atoms. The hierarchy in the chemical bonding, established by the difference in the bond strengths of Cs-Cu/S and Cu-S, contributes favorably to the reduction of the thermal conductivity in *o*-CsCu<sub>5</sub>S<sub>3</sub> [68, 69]. Moreover, the overlapping charge cloud between Cu and S atoms in the [Cu<sub>5</sub>S<sub>3</sub>]<sup>−</sup> unit reveals the existence of Cu-S covalent bonds, as shown by the charge density equipotential surface. Conversely, the non-overlapping charge sphere around the Cs<sup>+</sup> ion implies the absence of the covalent bond, which corroborates the small IFC values of the Cs-Cu and Cs-S atoms.

## 4.2 Non-covalent interaction and metavalent bonding

The comprehensive chemical bonding research enables the understanding of potential lattice anharmonicity. A sophisticated approach to disclose the interatomic interaction is the non-covalent interaction (NCI) index, which relies on the electron density  $\rho$ , and its derivatives [70]. The NCI index employs the IRI based on the optimized reduced density gradients (RDG), a function of  $\text{sign}(\lambda_2)\rho$ , where  $\text{sign}(\lambda_2)$  denotes the sign of the second eigenvalue of the electron density Hessian matrix [70, 71]. Generally, the attractive (or bonding) interactions are indicated by negative  $\text{sign}(\lambda_2)\rho$  values. In the region of low electron density, a typical feature of weak interaction is a spike with a large change in RDG near zero at the critical point. In Fig. 2(a), partial vdW interactions, approaching zero ( $|\text{sign}(\lambda_2)\rho| < 0.001 \text{ a.u.}$ ), are present at the critical point within the low electron density region. At the same time, there is also a lot of bonding tending to be covalent ( $\text{sign}(\lambda_2)\rho < -0.002 \text{ a.u.}$ ).

Another key is to determine how the different interactions are distributed in *o*-CsCu<sub>5</sub>S<sub>3</sub>. Fig. 2(b) shows 3D IRI isosurfaces with BGR color scales that indicate the  $\text{sign}(\lambda_2)\rho$  values. As expected, the 2D [Cu<sub>5</sub>S<sub>3</sub>]<sup>−</sup> and Cs<sup>+</sup> layers are predominantly interspersed with weak van der Waals interactions, which facilitate the stochastic oscillation of Cs atoms as rattlers. In addition, the intralayer Cu–S interactions display a strong covalent character within the [Cu<sub>5</sub>S<sub>3</sub>]<sup>−</sup> slab, whereas



the red area surrounding the bonding reveals the existence of steric effects.

The degree of interlayer Cu-S covalency can be assessed by calculating the shared and transferred charges located in the 2D bonding mechanism diagram [72] in Fig. 2(c). With a shared charge and a transferred charge of  $0.8|e|$  and  $0.55|e|$ , respectively, the intermediate electron behavior exhibits the metavalent bond. Such specific metavalent bonding tends to induce moderate electrical conductivity, large optical permittivity, and strong lattice anharmonicity (larger mode-specific Grüneisen parameter ( $\gamma_i$ ) associated with the optical phonons) [72, 73, 74]. In fact, the material investigated here resides in the domain of the metavalent bond together with other renowned low- $\kappa_L$  thermoelectric materials, such as PbTe [75], AgBiTe<sub>2</sub> [76], and so on [77]. Consequently, the severe limitation of the propagation of thermal phonons results from the coexistence of elementary valence bonds and random oscillations of Cs atoms.

### 4.3 Anharmonically re-normalized phonons

**Anharmonic lattice dynamics.** In functional materials, both the cubic and quartic anharmonicities are essential for the accurate modeling of lattice dynamics. For crystalline o-CsCu<sub>5</sub>S<sub>3</sub>, 0-K phonon dispersions and the anharmonically renormalized phonon dispersions arising from bubble and loop diagrams [78] at finite temperatures are illustrated in Fig. 2(a). When considering the effect of higher-order anharmonic phonon-phonon interaction on phonon dispersions [79], distinctive phonon energy shifts were observed in o-CsCu<sub>5</sub>S<sub>3</sub> [see Fig. 3(a)]. Although the low-frequency optical modes undergo slight hardening or softening, the high-frequency optical modes experience significant softening. As indicated by the anharmonic phonon density of states and atomic participation ratio [see Figs. 3(a-c)], the hardening low-frequency modes are mainly dominated by the Cs atoms. The hardening behavior observed in Cs-dominated modes can be attributed to weakly bound Cs atoms oscillating randomly as rattlers, which can be reflected by the large mean-square atomic displacements (MSDs) [80, 81]. In addition, the significant softening in high-frequency modes is primarily contributed by S atoms, as indicated in Fig. 3(a). The softening phenomenon in high-frequency optical modes has also been observed in other highly anharmonic compounds, including CsCu<sub>2</sub>I<sub>3</sub> [82] and

BaZrO<sub>3</sub> [83, 84].

Considering only the effect of quartic anharmonicity, i.e., loop self-energy, on phonon energy shifts may lead to an overestimation issue in highly anharmonic materials [48, 84]. A notable hardening trend is observed across the almost entire phonon spectrum with increasing temperature. [see Fig. S2] However, accounting for the effect of cubic anharmonicity, i.e., bubble self-energy, on phonon energy shifts dramatically suppresses the phonon hardening, owing to negative frequency shifts from the bubble diagram [see Fig. 3 (a)]. This observation indicates the comparable roles played by cubic and quartic anharmonicities in influencing phonon energy shifts in *o*-CsCu<sub>5</sub>S<sub>3</sub>. Therefore, the competition between the quartic anharmonicity and the cubic anharmonicity accounts for the predicted phonon softening of *o*-CsCu<sub>5</sub>S<sub>3</sub>. More importantly, an accurate lattice dynamics modeling is essential for investigating the properties of thermal transport, which will be discussed later.

In addition, the dispersive low-lying optical (LLO) branch manifests avoided crossings with the longitudinal acoustic (LA) branch, as the indication of phonon polarization hybridization. [see Fig. S3] Traditionally, the phonon group velocities near the avoided crossing points are suppressed, thereby constraining the transport efficiency of heat-carrying phonons [85, 86]. Other research has pointed out that optical-acoustic phonon coupling can also enhance scattering rates and suppress lattice thermal conductivity through the hybridization of optical phonon eigenvectors into acoustic phonons [87]. Meanwhile, numerous flattened low-frequency optical branches with soft vibrations act as Einstein oscillators, which have also been demonstrated to be advantageous for phonon scattering [88, 89, 90]. Similarly, these flattened branches are also associated with Cs atoms that exhibit random rattling motions [91]. These indices anticipate the existence of strong lattice anharmonicity, which can severely suppress the heat transport in the *o*-CsCu<sub>5</sub>S<sub>3</sub> crystals.

#### 4.4 Dual-channel thermal transport model

**Lattice thermal conductivity.** We next move on to calculate the total  $\kappa_L$  including the inherent solidlike (i.e., population conductivity  $\kappa_L^P$  from particlelike propagation) and glasslike (i.e., coherence conductivity  $\kappa_L^C$  from wavelike tunneling) terms within the framework of the

Wigner formalism of quantum mechanics [49, 50]. Among them, the  $\kappa_L^P$  concurs with the conventional Peierls-Boltzmann thermal conductivity in crystals derived from the diagonal terms ( $j = j'$ ) of the heat-flux operator. The off-diagonal terms ( $j \neq j'$ ) give rise to  $\kappa_L^C$ , as outlined by the Allen-Feldman equation for glasses. Particularly, when the phonon mean free path (MFP) approximates the interatomic spacing, these off-diagonal terms become significantly influential [92]. The combination of the phonon broadening and energy shifts considering both the cubic and quartic anharmonicity with non-diagonal terms of heat flux operators (OD), i.e., the SCPB+3,4ph+OD method, allows us to obtain reliable thermal conductivity. In Fig. 4(a), the converged  $\kappa_L$  at 300 K along the  $x$ - and  $z$ -directions reaches 0.42 and 0.38  $\text{Wm}^{-1}\text{K}^{-1}$ , respectively, in good agreement with the experimental values (0.35 ~ 0.50  $\text{Wm}^{-1}\text{K}^{-1}$ ). We note that the  $\kappa_{L,x}^P$  and  $\kappa_{L,z}^P$  exhibits the conventional negative correlation with temperature, attributed to the stronger phonon interactions at higher temperatures. On the contrary, the heating process witnesses a continuous rise trend of  $\kappa_{L,z}^C$  and its dominance over the total thermal transfer in  $z$  direction resulting from a strong approximate linear positive temperature response, while  $\kappa_{L,x}^C$  shows no sensitivity to temperature and remains almost stable in the same interval. Along its stacking direction, the calculated  $\kappa_{L,y}$  attains an exceedingly low value of 0.150  $\text{Wm}^{-1}\text{K}^{-1}$  [see Fig. S4], merely five times that of air (0.025  $\text{Wm}^{-1}\text{K}^{-1}$  at 300 K) [93]. Because its layered structure with the stacking of 2D  $[\text{Cu}_5\text{S}_3]^-$  and  $\text{Cs}^+$  layers is expected to result in small group velocity, thereby limiting heat transport of phonons outside the plane.

On the other hand, the coherent thermal conductivity surges with the elevation of temperature and progressively dominates in comparison to the population contribution, thereby considerably influencing the temperature dependence of the  $\kappa_L$ . Reproducing the experimentally observed ultra-low  $\kappa_L$  and weak dependence on temperature requires precise theoretical models, as illustrated in Fig. 4(b). To be specific, the heat conductance in  $o\text{-CsCu}_5\text{S}_3$  is revealed to exhibit glass-like characteristics as coherence contributions play a non-negligible role in the total  $\kappa_L$  over a wide range of temperatures. Considering only 3ph scattering processes, i.e., the SCP+3ph model, the predicted  $\kappa_L$  is about 0.62  $\text{Wm}^{-1}\text{K}^{-1}$  by averaging the values along the two principal crystallographic axes. It also exhibits an extremely weak temperature

dependence of  $T^{-0.55}$  in the 300-800 K range, which contradicts the conventional understanding of the  $T^{-1}$  dependence because of the consideration of anharmonic renormalization [94, 12]. However, the  $\kappa_L$  drops to around  $0.39 \text{ Wm}^{-1}\text{K}^{-1}$  and the temperature dependence of  $\kappa_L$  becomes stronger ( $T^{-0.85}$ ) by further taking into account additional negative phonon softening stemming from cubic anharmonicity. The value seems to match the experimental value at 300 K, but the error grows steadily with increasing temperature due to its strong temperature dependence. Then the  $\kappa_L$  is further reduced and the temperature dependence is also strengthened to  $T^{-1.38}$  with the introduction of 4ph scattering, which is significantly enhanced at high temperatures. Excitingly, the temperature dependence replicated experimentally observed well [33] ( $T^{-0.33}$  along with the parallel to the Bridgman growth direction) across the entire temperature range after we carry out a non-diagonalized correction to  $\kappa_L$ . Consequently, the state-of-the-art heat transport theory is essential for reproducing the experimental temperature dependence of  $\kappa_L$ , especially in glass-like and disordered crystals [95].

**Particle-like phonon transport properties.** Fig. 4(c) and Fig. 4(d) illustrate the phonon lifetime  $\tau(\mathbf{q})$  with respect to the phonon frequency at 300 K and 800 K, respectively. One can observe that the phonon lifetime is significantly reduced by the enhanced phonon scattering as the temperature rises. Simultaneously, the 4ph scattering processes effect becomes more prominent than the 3ph scattering processes, especially at 800 K, due to the high temperature activating more high-frequency thermal phonons to take part in the scattering. Notably, almost all phonons are above the approximate Ioffe-regel limit [96], i.e.,  $\tau(q) = [\Gamma(q)]^{-1} > 1/\omega(q)$ , which means that the theoretical framework for describing transport using the phonon quasiparticle excitation concept is valid. Furthermore, the timescale  $[\Delta\omega_{av}]^{-1}$  as “Wigner limit in time” can distinguish the relative contributions of particle-like and wave-like thermal transport mechanisms [50], wherein the phonon with  $\tau_{\text{Ioffe}} < \tau < \tau_{\text{Winger}}$  mainly influence to  $\kappa_L^C$ , while the phonon with  $\tau > \tau_{\text{Winger}}$  mainly contribute to  $\kappa_L^P$ . Even though only a small fraction of low-frequency phonons surpass the Winger criterion in lifetime, they are still the predominant thermal carriers at 300 K, because most mid- and high-frequency optical phonons are still in the “frozen” state. At 800 K, the heat is mainly transferred between phonon eigenstates via

interband tunneling because almost all phonons with a lifetime below the Wigner limit in time, which highlights the necessity of evoking the wave-like tunneling transport channel. Interestingly, we observe that 4ph scattering modifies the phonon lifetime in the frequency range from 50 to 130  $\text{cm}^{-1}$ , thus altering the way they propagate as heat carriers at 800 K.

In the traditional phonon gas diagram, the phonons are treated as discrete particles. The mode-specific contributions can be elucidated by examining the population conductivity spectrum  $\kappa_L^P(\omega)$  and corresponding cumulative, as shown in Fig. 5. The results reflect that  $\kappa_{L,x}^P$  and  $\kappa_{L,z}^P$  predominantly originate from acoustic and low-frequency optical modes ( $< 130 \text{ cm}^{-1}$ ). For the SCPB+3ph model, the low-frequency phonons are mainly scattered in the form of the combination process ( $W_{3ph}^+ : \lambda + \lambda' \rightarrow \lambda''$ ), which can be reflected in their weighted scattered phase space due to the constraint of energy conservation. [see Fig. S5] In addition, the high-frequency optical modes impart considerable contribution on  $\kappa_{L,x}^P$  but exert marginal impacts on  $\kappa_{L,z}^P$ , which can be traced back to the projection of the phonon velocity-operator in different directions. [see Fig. S6] After further consideration of 4ph scattering, the transport capacity of heat carriers in low-frequency regions (around 50  $\text{cm}^{-1}$ ) decreases obviously, especially at high temperatures, in which these modes mainly involve strong quartic anharmonic scattering induced by the rattling motion of Cs atoms. For 4ph scattering process, the redistribution process ( $\Gamma_{4ph}^{+-} : \lambda + \lambda' \rightarrow \lambda'' + \lambda'''$ ) maintains advantage for the low-frequency range because the  $\Gamma_{4ph}^{+-}$  process is more likely to satisfy the selection rule [97]. [see Fig. S7] More specifically, the numerous flat optical branches in the mid-high frequency region serve as mediums to assist in scattering as they can readily confine the scattering process to specific channels that conserve energy and momentum simultaneously [80, 17, 98].

**Wave-like phonon transport properties.** In contrast to the particle-like propagation, the interbranch generalized group velocity arises from the interplay of distinct phonon vibrational eigenstates [53]. The  $\kappa_{L,x}^C$  and  $\kappa_{L,z}^C$  exhibit indistinguishable values at ambient conditions, and they both depend on the coherent involvement of phonons with mid-low frequencies. To elucidate the different temperature dependence between  $\kappa_{L,x}^C$  and  $\kappa_{L,z}^C$  and the influence of coupled vibrational eigenstates on wave-like transport, we present the two-dimensional density

of state  $\kappa_{L,\omega_{jj}}^C$  for the coherence conductivity at 300 K and 800 K. [see Figs. 6(a-d)] Noteworthy, phonons with almost the same frequencies, i.e. quasi-degenerate vibrational eigenstates ( $\omega_{qj} \cong \omega_{qj}$ ) along the  $x$ - and  $z$ -directions, mainly dedicate the coherence conductivity at 300 K. Interestingly, the diagonal area is predominantly occupied by large values of  $\kappa_{L,\omega_{jj}}^C$ , especially for phonons with Cs rattling vibrations in the low-frequency region. These regions are associated with high rates of 4ph scattering, which can facilitate the coupling of the phonons with relatively large frequency differences [79]. At 800 K, non-degenerate phonon contributions prevail over as many mid-high frequency optical phonons are thermally activated, especially along the  $x$ -direction. We further show the spectral and cumulative coherences' thermal conductivity at 300 and 800 K, respectively. [see Figs. 6(e-d)] The frequency does not limit the contribution of  $\kappa_L^C$ , and it contributes significantly over almost the entire frequency range. Especially at 800 K,  $\kappa_{L,z}^C$  exhibits a sharp increase in the frequency range of 250-300  $\text{cm}^{-1}$ , which is mainly attributed to the contribution of non-degenerate phonon states in this region. This observation again emphasizes that further considering the coupled vibrational eigenstate can correctly reveal the origin of anomalous lattice thermal transport.

#### 4.5 Electronic transport and thermoelectric performance

**Electronic transport and properties.** The experimentally and theoretically observed exceptionally low thermal conductivity  $\kappa_L$  in  $o$ -CsCu<sub>5</sub>S<sub>3</sub> highlights its promising potential for application in thermoelectric devices. The electronic transport properties of  $o$ -CsCu<sub>5</sub>S<sub>3</sub> can be rigorously evaluated by conducting a theoretical analysis of its electronic band structure. [see Fig. S8] The theoretically observed high-lying valence band maximum and low ionization potential in  $o$ -CsCu<sub>5</sub>S<sub>3</sub> play a crucial role in facilitating the formation of hole carriers, a phenomenon demonstrated by prior experiments [33]. Therefore, fine-tuning the hole concentration can further enhance the attainment of optimal thermoelectric properties in  $o$ -CsCu<sub>5</sub>S<sub>3</sub>.

Fig. 7 illustrates the temperature-dependent characteristics of  $p$ -type electrical conductivity ( $\sigma$ ), Seebeck coefficient ( $S$ ), power factor (PF), and electronic thermal conductivity ( $\kappa_e$ ) for  $o$ -CsCu<sub>5</sub>S<sub>3</sub>. These electronic transport properties are computed across a range of charge carrier concentration from  $10^{18}$  to  $10^{21}$   $\text{cm}^{-3}$ . Generally, the covalent

bonds with the wider orbital overlap tend to facilitate the carrier transitions and ensure larger conductivity. As expected, the metavalence bond in *o*-CsCu<sub>5</sub>S<sub>3</sub> cannot achieve very ideal conductivity because it deviates from the perfect covalence bond [99]. Among the carrier scattering mechanisms, we note that the scattering of polar optical phonons to carriers has the largest perturbation of charge carriers across the whole range, which severely limits the mobility of electrons. [see Fig. S9] In addition, an environment with lower temperatures and higher carrier concentrations ensures that maximum conductivity ( $\sim 21.9 \times 10^4 \text{ Sm}^{-1}$ ) is achieved as the lower temperatures can reduce the scattering of carriers while higher concentrations enhance the overall electrical transport capacity. Meanwhile, the electronic thermal conductivity  $\kappa_e$  is positively correlated with the conductivity  $\sigma$ , which can be described as Wiedemann-Franz law [100] ( $\kappa_e = L\sigma T$ , where  $L$  is the Lorenz number). Accordingly, they show a similar distribution on the heat map. For Seebeck coefficient  $S$ , it usually shows the opposite trend to electrical conductivity, therefore, its maximum value reaches  $672 \mu\text{VK}^{-1}$  at  $10^{21} \text{ cm}^{-3}$  and 800 K. Notably, the narrow energy gap between the VBM and the secondary valence band (VBM<sub>2</sub>) ensures the electronic states near the Fermi surface [6, 101]. Consequently, a high value of  $S$  can be obtained from a high-valley multiplicity in the *p*-type *o*-CsCu<sub>5</sub>S<sub>3</sub>. Finally, the theoretical maximum power factor is achieved with  $1.48 \text{ mWm}^{-1}\text{K}^{-1}$  at 800 K and carrier concentration of  $3.86 \times 10^{20} \text{ cm}^{-3}$  under the competitive relationship between electron transport parameters.

**Thermoelectric conversion efficiency.** To achieve the maximum thermoelectric value  $ZT$ , it is imperative to intricately balance the interrelationships among various electronic transport parameters. In Fig. 8(a), the peak  $ZT$  values for *o*-CsCu<sub>5</sub>S<sub>3</sub> are identified as 1.88 at 800 K, aligning with optimal charge carrier concentrations of  $5.74 \times 10^{19} \text{ cm}^{-3}$ . Assuming that the required optimal carrier concentrations can be achieved through doping, *p*-type *o*-CsCu<sub>5</sub>S<sub>3</sub> emerges as a highly promising material for high-temperature thermoelectric applications, given its high  $ZT$  values and phase transition temperature. In the realm of thermoelectric materials, the conversion efficiency  $\eta$  is recognized as a practical indicator for evaluating thermoelectric performance. Typically, a conversion efficiency of no less than 15% is required for thermoelectric devices to meet the crucial criterion for market applica-

tions [102]. Fig. 8(b) illustrates the conversion efficiency  $\eta$ , wherein the hot end temperature spans from 400 to 800 K, and the cold end temperature defaults to 300 K. The optimal conversion efficiency  $\eta$  of 18.4% is achieved at the same temperature and carrier concentration corresponding to the maximum ZT value. This serves as additional confirmation of its potential practical application value.

## 5 Conclusions

In conclusion, we have systematically investigated the microscopic mechanisms of thermal transport in crystalline  $o$ -CsCu<sub>5</sub>S<sub>3</sub> by using a first-principles-based anharmonic phonon renormalization and linearized Wigner transport equation. Our findings highlight the essential role played by both the cubic and quartic anharmonicities in accurately modeling the lattice dynamics and thermal transport in  $o$ -CsCu<sub>5</sub>S<sub>3</sub>. Specifically, the negative phonon energy shifts from the bubble diagram are indispensable for accurately capturing the anharmonic lattice dynamics. Using a dual-channel thermal transport channel considering contributions from both three- and four-phonon scatterings, we can well reproduce the experimentally measured ultra-low thermal conductivity and its glassy-like temperature dependence. Furthermore, our findings demonstrate that the combination of weakly bound Cs atoms with a strong chemical bond hierarchy between Cu and S atoms leads to the coexistence of fluctuating noncrystalline rattlers and metavalent bonding in  $o$ -CsCu<sub>5</sub>S<sub>3</sub>. This structural arrangement constrains particle-like phonon propagation while enhancing the wave-like tunneling of phonons. Concretely, strong phonon broadening leads to a strong coupling between inter-branch coherent vibration eigenstates with increasing temperature, which causes a transformation from particle-like wave packet propagation to wavelike phonon transport in the dominance of heat transport. In addition, the electrical transport properties are determined by applying a precise momentum relaxation-time approximation within the framework of the linearized Boltzmann transport equation. A maximum thermoelectric value ZT of 1.88 and conversion efficiency of 18.4% observed at 800 K  $p$ -type  $o$ -CsCu<sub>5</sub>S<sub>3</sub> is achieved by properly adjusting the carrier concentration, which confirms its potential advantages in the field of thermoelectric materials. Our work provides a microscopic explanation of the glass-like thermal conductivity and further facilitates the development of anharmonic lattice dynamics while highlighting the values of application as potential  $p$ -type thermoelectric



materials in  $o$ -CsCu<sub>5</sub>S<sub>3</sub>.

### **Author Contributions**

The authors confirm their contribution to the paper as follows: writing - original draft : J.C.Y. and J.Z.Z.; conceptualization : J.Z.Z; data curation : J.C.Y., J.D.L., and W.L.R; investigation: S.Q.G and H.L.; writing - review & editing : Y.H.L and T.C.; funding acquisition : T.C. All authors reviewed the results and approved the final version of the manuscript.

### **Conflicts of interest**

There are no conflicts to declare.

### **Acknowledgements**

This work was supported by the National Natural Science Foundation of China (Grant No. 52072188, No. 12204254), the Program for Science and Technology Innovation Team in Zhejiang (Grant No. 2021R01004), and the Natural Science Foundation of Zhejiang province (Grant No. LQ23A040005). We are grateful to the Institute of High-pressure Physics of Ningbo University for its computational resources.

### **References**

- 1 M. Massetti, F. Jiao, A. J. Ferguson, D. Zhao, K. Wijeratne, A. Würger, J. L. Blackburn, X. Crispin, S. Fabiano, Unconventional thermoelectric materials for energy harvesting and sensing applications, *Chem. Rev.* 121 (20) (2021) 12465–12547.
- 2 B. Russ, A. Glauddell, J. J. Urban, M. L. Chabinye, R. A. Segalman, Organic thermoelectric materials for energy harvesting and temperature control, *Nat. Rev. Mater.* 1 (10) (2016) 1–14.
- 3 W. G. Zeier, J. Schmitt, G. Hautier, U. Aydemir, Z. M. Gibbs, C. Felser, G. J. Snyder, Engineering half-Heusler thermoelectric materials using Zintl chemistry, *Nat. Rev. Mater.* 1 (6) (2016) 1–10.
- 4 G. Tan, L.-D. Zhao, M. G. Kanatzidis, Rationally designing high-performance bulk thermoelectric materials, *Chem. Rev.* 116 (19) (2016) 12123–12149.
- 5 C. Wan, X. Gu, F. Dang, T. Itoh, Y. Wang, H. Sasaki, M. Kondo, K. Koga, K. Yabuki, G. J. Snyder, et al., Flexible n-type thermoelectric materials by organic intercalation of layered transition metal dichalcogenides, *Nat. Mater.* 14 (6) (2015) 622–627.

- 6 Y. Pei, X. Shi, A. LaLonde, H. Wang, L. Chen, G. J. Snyder, Convergence of electronic bands for high performance bulk thermoelectrics, *Nature* 473 (7345) (2011) 66–69.
- 7 Y. Tang, Z. M. Gibbs, L. A. Agapito, G. Li, H.-S. Kim, M. B. Nardelli, S. Curtarolo, G. J. Snyder, Convergence of multi-valley bands as the electronic origin of high thermoelectric performance in cosb3 skutterudites, *Nat. Mater.* 14 (12) (2015) 1223–1228.
- 8 C. Xiao, Z. Li, K. Li, P. Huang, Y. Xie, Decoupling interrelated parameters for designing high performance thermoelectric materials, *Acc. Chem. Res.* 47 (4) (2014) 1287–1295.
- 9 K. Zhao, E. Eikeland, D. He, W. Qiu, Z. Jin, Q. Song, T.-r. Wei, P. Qiu, J. Liu, J. He, et al., Thermoelectric materials with crystal-amorphicity duality induced by large atomic size mismatch, *Joule* 5 (5) (2021) 1183–1195.
- 10 J. Yue, S. Guo, J. Li, J. Zhao, C. Shen, H. Zhang, Y. Liu, T. Cui, Pressure-induced remarkable four-phonon interaction and enhanced thermoelectric conversion efficiency in cuinte2, *Mater. Today Phys.* 39 (2023) 101283.
- 11 J. Yue, A. Zhang, J. Li, Y. Liu, T. Cui, Significantly reinforced thermoelectric performance in the novel 1t-au6se2 monolayer, *APL Mater.* 11 (3) (2023).
- 12 M. Beekman, D. T. Morelli, G. S. Nolas, Better thermoelectrics through glass-like crystals, *Nat. Mater.* 14 (12) (2015) 1182–1185.
- 13 J. R. Sootsman, D. Y. Chung, M. G. Kanatzidis, New and old concepts in thermoelectric materials, *Angew. Chem. Int. Ed.* 48 (46) (2009) 8616–8639.
- 14 X.-Y. Mi, X. Yu, K.-L. Yao, X. Huang, N. Yang, J.-T. Lü, Enhancing the thermoelectric figure of merit by low-dimensional electrical transport in phonon-glass crystals, *Nano Lett.* 15 (8) (2015) 5229–5234.
- 15 S. Guo, Y. Liu, T. Cui, et al., Novel room-temperature full-heusler thermoelectric material li2tlsb, *Phys. Chem. Chem. Phys.* (2024).

- 16 J. J. Plata, E. J. Blancas, A. M. Márquez, V. Posligua, J. F. Sanz, R. Grau-Crespo, Harnessing the unusually strong improvement of thermoelectric performance of aginte 2 with nanostructuring, *J. Mater. Chem. A* 11 (31) (2023) 16734–16742.
- 17 J. Zheng, D. Shi, S. Liu, Y. Yang, C. Lin, Z. Chang, R. Guo, B. Huang, Effects of high-order anharmonicity on anomalous lattice dynamics and thermal transport in fully filled skutterudite ybfe 4 sb 12, *Phys. Rev. Mater.* 6 (9) (2022) 093801.
- 18 M. K. Jana, K. Pal, A. Warankar, P. Mandal, U. V. Waghmare, K. Biswas, Intrinsic rattler-induced low thermal conductivity in zintl type tlnte2, *J. Am. Chem. Soc* 139 (12) (2017) 4350–4353.
- 19 Z.-G. Chen, X. Shi, L.-D. Zhao, J. Zou, High-performance sntse thermoelectric materials: Progress and future challenge, *Prog. Mater. Sci.* 97 (2018) 283–346.
- 20 H. Liu, X. Shi, F. Xu, L. Zhang, W. Zhang, L. Chen, Q. Li, C. Uher, T. Day, G. J. Snyder, Copper ion liquid-like thermoelectrics, *Nat. Mater.* 11 (5) (2012) 422–425.
- 21 T. Tadano, S. Tsuneyuki, Quartic anharmonicity of rattlers and its effect on lattice thermal conductivity of clathrates from first principles, *Phys. Rev. Lett.* 120 (10) (2018) 105901.
- 22 K. Zhao, A. B. Blichfeld, H. Chen, Q. Song, T. Zhang, C. Zhu, D. Ren, R. Hanus, P. Qiu, B. B. Iversen, et al., Enhanced thermoelectric performance through tuning bonding energy in cu2se1-x s x liquid-like materials, *Chem. Mater.* 29 (15) (2017) 6367–6377.
- 23 Z. Zhang, K. Zhao, T.-R. Wei, P. Qiu, L. Chen, X. Shi, Cu 2 se-based liquid-like thermoelectric materials: looking back and stepping forward, *Energy Environ. Sci.* 13 (10) (2020) 3307–3329.
- 24 A. J. Rettie, C. D. Malliakas, A. S. Botana, J. M. Hodges, F. Han, R. Huang, D. Y. Chung, M. G. Kanatzidis, Ag2se to kag3se2: suppressing order–disorder transitions via reduced dimensionality, *J. Am. Chem. Soc.* 140 (29) (2018) 9193–9202.
- 25 C. Wang, R. Cheng, Y. Chen, Theoretical evaluation of the persistence of transverse phonons across a liquid-like transition in

- superionic conductor  $\text{KAg}_3\text{Se}_2$ , *Chem. Mater.* 35 (4) (2023) 1780–1787.
- 26 B. Li, H. Wang, Y. Kawakita, Q. Zhang, M. Feygenson, H. Yu, D. Wu, K. Ohara, T. Kikuchi, K. Shibata, et al., Liquid-like thermal conduction in intercalated layered crystalline solids, *Nat. Mater.* 17 (3) (2018) 226–230.
- 27 G. Dennler, R. Chmielowski, S. Jacob, F. Capet, P. Roussel, S. Zastrow, K. Nielsch, I. Opahle, G. K. Madsen, Are binary copper sulfides/selenides really new and promising thermoelectric materials?, *Adv. Energy Mater.* 4 (9) (2014) 1301581.
- 28 K. Zhao, P. Qiu, X. Shi, L. Chen, Recent advances in liquid-like thermoelectric materials, *Adv. Funct. Mater.* 30 (8) (2020) 1903867.
- 29 N. Ma, Y.-Y. Li, L. Chen, L.-M. Wu,  $\alpha\text{-Cu}_5\text{Se}_3$ : discovery of a low-cost bulk selenide with high thermoelectric performance, *J. Am. Chem. Soc.* 142 (11) (2020) 5293–5303.
- 30 Y. He, T. Day, T. Zhang, H. Liu, X. Shi, L. Chen, G. J. Snyder, High thermoelectric performance in non-toxic earth-abundant copper sulfide, *Adv. Mater.* 26 (23) (2014) 3974–3978.
- 31 Z. Xia, H. Fang, X. Zhang, M. S. Molochev, R. Gautier, Q. Yan, S.-H. Wei, K. R. Poeppelmeier,  $\text{Cu}_5\text{Se}_3$ : A copper-rich ternary chalcogenide semiconductor with nearly direct band gap for photovoltaic application, *Chem. Mater.* 30 (3) (2018) 1121–1126.
- 32 C. Yang, Z. Wang, Y. Lv, R. Yuan, Y. Wu, W.-H. Zhang, Colloidal  $\text{Cu}_5\text{S}_3$  nanocrystals as an interlayer in high-performance perovskite solar cells with an efficiency of 22.29%, *Chem. Eng. J.* 406 (2021) 126855.
- 33 N. Ma, F. Jia, L. Xiong, L. Chen, Y.-Y. Li, L.-M. Wu,  $\text{Cu}_5\text{S}_3$ : promising thermoelectric material with enhanced phase transition temperature, *Inorg. Chem.* 58 (2) (2019) 1371–1376.
- 34 G. Kresse, J. Furthmüller, Efficient iterative schemes for ab initio total-energy calculations using a plane-wave basis set, *Phys. Rev. B* 54 (16) (1996) 11169.

- 35 G. Kresse, J. Furthmüller, Efficiency of ab-initio total energy calculations for metals and semiconductors using a plane-wave basis set, *Comput. Mater. Sci.* 6 (1) (1996) 15–50.
- 36 G. Kresse, D. Joubert, From ultrasoft pseudopotentials to the projector augmented-wave method, *Phys. Rev. B* 59 (3) (1999) 1758.
- 37 J. P. Perdew, K. Burke, M. Ernzerhof, Generalized gradient approximation made simple, *Phys. Rev. Lett.* 77 (18) (1996) 3865.
- 38 J. Klimeš, D. R. Bowler, A. Michaelides, Van der waals density functionals applied to solids, *Phys. Rev. B* 83 (19) (2011) 195131.
- 39 K. Esfarjani, H. T. Stokes, Method to extract anharmonic force constants from first principles calculations, *Phys. Rev. B* 77 (14) (2008) 144112.
- 40 F. Zhou, W. Nielson, Y. Xia, V. Ozoliņš, et al., Lattice anharmonicity and thermal conductivity from compressive sensing of first-principles calculations, *Phys. Rev. Lett.* 113 (18) (2014) 185501.
- 41 F. Zhou, W. Nielson, Y. Xia, V. Ozoliņš, et al., Compressive sensing lattice dynamics. i. general formalism, *Phys. Rev. B* 100 (18) (2019) 184308.
- 42 F. Zhou, B. Sadigh, D. Åberg, Y. Xia, V. Ozoliņš, et al., Compressive sensing lattice dynamics. ii. efficient phonon calculations and long-range interactions, *Phys. Rev. B* 100 (18) (2019) 184309.
- 43 L. J. Nelson, G. L. Hart, F. Zhou, V. Ozoliņš, et al., Compressive sensing as a paradigm for building physics models, *Phys. Rev. B*.
- 44 T. Tadano, S. Tsuneyuki, Self-consistent phonon calculations of lattice dynamical properties in cubic srtio 3 with first-principles anharmonic force constants, *Phys. Rev. B* 92 (5) (2015) 054301.
- 45 T. Tadano, Y. Gohda, S. Tsuneyuki, Anharmonic force constants extracted from first-principles molecular dynamics: applications to heat transfer simulations, *J. Phys. Condens. Matter* 26 (22) (2014) 225402.

- 46 I. Errea, B. Rousseau, A. Bergara, Anharmonic stabilization of the high-pressure simple cubic phase of calcium, *Phys. Rev. Lett.* 106 (16) (2011) 165501.
- 47 Y. Xia, V. Ozoliņš, C. Wolverton, Microscopic mechanisms of glasslike lattice thermal transport in cubic  $\text{Cu}_2\text{Sb}$  tetrahedrites, *Phys. Rev. Lett.* 125 (8) (2020) 085901.
- 48 T. Tadano, W. A. Saidi, First-principles phonon quasiparticle theory applied to a strongly anharmonic halide perovskite, *Phys. Rev. Lett.* 129 (18) (2022) 185901.
- 49 M. Simoncelli, N. Marzari, F. Mauri, Unified theory of thermal transport in crystals and glasses, *Nat. Phys.* 15 (8) (2019) 809–813.
- 50 M. Simoncelli, N. Marzari, F. Mauri, Wigner formulation of thermal transport in solids, *Phys. Rev. X* 12 (4) (2022) 041011.
- 51 Y. Xia, K. Pal, J. He, V. Ozoliņš, C. Wolverton, Particlelike phonon propagation dominates ultralow lattice thermal conductivity in crystalline  $\text{Ti}_3\text{VSe}_4$ , *Phys. Rev. Lett.* 124 (6) (2020) 065901.
- 52 S.-i. Tamura, Isotope scattering of dispersive phonons in  $\text{Ge}$ , *Phys. Rev. B* 27 (2) (1983) 858.
- 53 P. B. Allen, J. L. Feldman, Thermal conductivity of disordered harmonic solids, *Physical Review B* 48 (17) (1993) 12581.
- 54 W. Li, J. Carrete, N. A. Katcho, N. Mingo, Shengbte: A solver of the boltzmann transport equation for phonons, *Comput. Phys. Commun.* 185 (6) (2014) 1747–1758.
- 55 Z. Han, X. Yang, W. Li, T. Feng, X. Ruan, Fourphonon: An extension module to shengbte for computing four-phonon scattering rates and thermal conductivity, *Comput. Phys. Commun.* 270 (2022) 108179.
- 56 A. M. Ganose, J. Park, A. Faghaninia, R. Woods-Robinson, K. A. Persson, A. Jain, Efficient calculation of carrier scattering rates from first principles, *Nat. Commun.* 12 (1) (2021) 2222.

- 57 M. Born, Quantenmechanik der stoßvorgänge, *Z. Med. Phys.* 38 (11-12) (1926) 803–827.
- 58 H. Fröhlich, Electrons in lattice fields, *Adv. Phys.* 3 (11) (1954) 325–361.
- 59 H. Brooks, Scattering by ionized impurities in semiconductors, in: *Phys. Rev.*, Vol. 83, AMERICAN PHYSICAL SOC ONE PHYSICS ELLIPSE, COLLEGE PK, MD 20740-3844 USA, 1951, pp. 879–879.
- 60 T. A. Manz, N. G. Limas, Introducing ddec6 atomic population analysis: part 1. charge partitioning theory and methodology, *RSC adv.* 6 (53) (2016) 47771–47801.
- 61 N. G. Limas, T. A. Manz, Introducing ddec6 atomic population analysis: part 2. computed results for a wide range of periodic and nonperiodic materials, *RSC adv.* 6 (51) (2016) 45727–45747.
- 62 T. A. Manz, Introducing ddec6 atomic population analysis: part 3. comprehensive method to compute bond orders, *RSC adv.* 7 (72) (2017) 45552–45581.
- 63 T. Lu, F. Chen, Multiwfn: A multifunctional wavefunction analyzer, *J. Comput. Chem.* 33 (5) (2012) 580–592.
- 64 T. Lu, Q. Chen, Interaction region indicator: A simple real space function clearly revealing both chemical bonds and weak interactions, *Chemistry-Methods* 1 (5) (2021) 231–239.
- 65 C. Weedbrook, S. Pirandola, R. García-Patrón, N. J. Cerf, T. C. Ralph, J. H. Shapiro, S. Lloyd, Gaussian quantum information, *Rev. Mod. Phys.* 84 (2) (2012) 621.
- 66 S. Manzetti, T. Lu, The geometry and electronic structure of aristolochic acid: possible implications for a frozen resonance, *J. Phys. Org. Chem.* 26 (6) (2013) 473–483.
- 67 Y. Chen, Y. Shen, X. Li, J. Sun, Q. Wang,  $\beta$ -cscu5se3: A promising thermoelectric material going beyond photovoltaic application, *Adv. Theory Simul.* 3 (11) (2020) 2000169.
- 68 L.-D. Zhao, S.-H. Lo, Y. Zhang, H. Sun, G. Tan, C. Uher, C. Wolverton, V. P. Dravid, M. G. Kanatzidis, Ultralow thermal conductivity

and high thermoelectric figure of merit in snse crystals, *Nature* 508 (7496) (2014) 373–377.

- 69 A. Bhui, T. Ghosh, K. Pal, K. Singh Rana, K. Kundu, A. Soni, K. Biswas, Intrinsically low thermal conductivity in the n-type vacancy-ordered double perovskite  $\text{Cs}_2\text{SnI}_6$ : octahedral rotation and anharmonic rattling, *Chem. Mater.* 34 (7) (2022) 3301–3310.
- 70 E. R. Johnson, S. Keinan, P. Mori-Sánchez, J. Contreras-García, A. J. Cohen, W. Yang, Revealing noncovalent interactions, *J. Am. Chem. Soc.* 132 (18) (2010) 6498–6506.
- 71 J. Contreras-García, E. R. Johnson, S. Keinan, R. Chaudret, J.-P. Piquemal, D. N. Beratan, W. Yang, Nciplot: a program for plotting noncovalent interaction regions, *J. Chem. Theory Comput.* 7 (3) (2011) 625–632.
- 72 B. J. Kooi, M. Wuttig, Chalcogenides by design: functionality through metavalent bonding and confinement, *Adv. Mater.* 32 (21) (2020) 1908302.
- 73 L. Guarneri, S. Jakobs, A. von Hoegen, S. Maier, M. Xu, M. Zhu, S. Wahl, C. Teichrib, Y. Zhou, O. Cojocaru-Miréidin, et al., Metavalent bonding in crystalline solids: how does it collapse?, *Adv. Mater.* 33 (39) (2021) 2102356.
- 74 J.-Y. Raty, M. Schumacher, P. Golub, V. L. Deringer, C. Gatti, M. Wuttig, A quantum-mechanical map for bonding and properties in solids, *Adv. Mater.* 31 (3) (2019) 1806280.
- 75 A. Romero, E. Gross, M. Verstraete, O. Hellman, Thermal conductivity in pbte from first principles, *Phys. Rev. B* 91 (21) (2015) 214310.
- 76 G. Tan, F. Shi, H. Sun, L.-D. Zhao, C. Uher, V. P. Dravid, M. G. Kanatzidis,  $\text{SnTe}$ - $\text{AgBiTe}_2$  as an efficient thermoelectric material with low thermal conductivity, *J. Mater. Chem. A* 2 (48) (2014) 20849–20854.
- 77 D. Sarkar, S. Roychowdhury, R. Arora, T. Ghosh, A. Vasdev, B. Joseph, G. Sheet, U. V. Waghmare, K. Biswas, Metavalent



bonding in gese leads to high thermoelectric performance, *Angew. Chem. Int. Ed.* 60 (18) (2021) 10350–10358.

- 78 G. P. Srivastava, *The physics of phonons*, CRC press, 2022.
- 79 J. Zheng, C. Lin, C. Lin, R. Guo, B. Huang, Strong anharmonic phonon renormalization and dominant role of wave-like tunnelling of phonons in thermal transport in lead-free halide double perovskites, arXiv preprint arXiv:2301.12273 (2023).
- 80 W. Li, N. Mingo, Ultralow lattice thermal conductivity of the fully filled skutterudite  $\text{YbFe}_4\text{Sb}_{12}$  due to the flat avoided-crossing filler modes, *Phys. Rev. B* 91 (14) (2015) 144304.
- 81 P. Acharyya, T. Ghosh, K. Pal, K. S. Rana, M. Dutta, D. Swain, M. Etter, A. Soni, U. V. Waghmare, K. Biswas, Glassy thermal conductivity in  $\text{Cs}_3\text{Bi}_2\text{I}_6\text{Cl}_3$  single crystal, *Nat. Commun.* 13 (1) (2022) 5053.
- 82 J. Zheng, C. Lin, C. Lin, B. Huang, R. Guo, G. Hautier, Wave-like tunneling of phonons dominates glass-like thermal transport in quasi-1d copper halide  $\text{CsCu}_2\text{I}_3$ , arXiv preprint arXiv:2310.13680 (2023).
- 83 C. Toulouse, D. Amoroso, C. Xin, P. Veber, M. C. Hatnean, G. Balakrishnan, M. Maglione, P. Ghosez, J. Kreisel, M. Guennou, Lattice dynamics and raman spectrum of  $\text{BaZrO}_3$  single crystals, *Phys. Rev. B* 100 (13) (2019) 134102.
- 84 J. Zheng, D. Shi, Y. Yang, C. Lin, H. Huang, R. Guo, B. Huang, Anharmonicity-induced phonon hardening and phonon transport enhancement in crystalline perovskite  $\text{BaZrO}_3$ , *Phys. Rev. B* 105 (22) (2022) 224303.
- 85 J. Li, W. Hu, J. Yang, High-throughput screening of rattling-induced ultralow lattice thermal conductivity in semiconductors, *J. Am. Chem. Soc.* 144 (10) (2022) 4448–4456.
- 86 J. Cohn, G. Nolas, V. Fessatidis, T. Metcalf, G. Slack, Glasslike heat conduction in high-mobility crystalline semiconductors, *Phys. Rev. Lett.* 82 (4) (1999) 779.

- 87 W. Li, J. Carrete, G. K. Madsen, N. Mingo, Influence of the optical-acoustic phonon hybridization on phonon scattering and thermal conductivity, *Phys. Rev. B* 93 (20) (2016) 205203.
- 88 J. Li, L. Wei, Z. Ti, L. Ma, Y. Yan, G. Zhang, P.-F. Liu, Wavelike tunneling of phonons dominates glassy thermal conductivity in crystalline  $\text{Cs}_3\text{Bi}_2\text{I}_6\text{Cl}_3$ , *Phys. Rev. B* 108 (22) (2023) 224302.
- 89 H. Liu, J. Yang, X. Shi, S. A. Danilkin, D. Yu, C. Wang, W. Zhang, L. Chen, Reduction of thermal conductivity by low energy multi-einstein optic modes, *J. Materiomics* 2 (2) (2016) 187–195.
- 90 V. Keppens, D. Mandrus, B. C. Sales, B. Chakoumakos, P. Dai, R. Coldea, M. Maple, D. Gajewski, E. Freeman, S. Bennington, Localized vibrational modes in metallic solids, *Nature* 395 (6705) (1998) 876–878.
- 91 Q.-Y. Xie, P.-F. Liu, J.-J. Ma, L.-M. Wu, K.-W. Zhang, B.-T. Wang, Microscopic mechanisms of glasslike lattice thermal conductivity in tetragonal  $\alpha\text{-CsCu}_5\text{Se}_3$ , *Phys. Rev. B* 108 (1) (2023) 014302.
- 92 Y. Luo, X. Yang, T. Feng, J. Wang, X. Ruan, Vibrational hierarchy leads to dual-phonon transport in low thermal conductivity crystals, *Nat. Commun.* 11 (1) (2020) 2554.
- 93 K. Stephan, A. Laesecke, The thermal conductivity of fluid air, *J. Phys. Chem. Ref. Data* 14 (1) (1985) 227–234.
- 94 Y. Xia, V. I. Hegde, K. Pal, X. Hua, D. Gaines, S. Patel, J. He, M. Aykol, C. Wolverton, High-throughput study of lattice thermal conductivity in binary rocksalt and zinc blende compounds including higher-order anharmonicity, *Phys. Rev. X* 10 (4) (2020) 041029.
- 95 S. Shenogin, A. Bodapati, P. Keblinski, A. J. McGaughey, Predicting the thermal conductivity of inorganic and polymeric glasses: The role of anharmonicity, *J. Appl. Phys.* 105 (3) (2009).
- 96 S. E. Skipetrov, I. Sokolov, Ioffe-regel criterion for anderson localization in the model of resonant point scatterers, *Phys. Rev. B* 98 (6) (2018) 064207.

- 97 N. K. Ravichandran, D. Broido, Phonon-phonon interactions in strongly bonded solids: selection rules and higher-order processes, *Phys. Rev. X* 10 (2) (2020) 021063.
- 98 L. Xie, J. Feng, R. Li, J. He, First-principles study of anharmonic lattice dynamics in low thermal conductivity agrse 2: evidence for a large resonant four-phonon scattering, *Phys. Rev. Lett.* 125 (24) (2020) 245901.
- 99 J. Yue, Y. Liu, W. Ren, S. Lin, C. Shen, H. K. Singh, T. Cui, T. Terumasa, H. Zhang, Role of atypical temperature-responsive lattice thermal transport on the thermoelectric properties of antiperovskites  $\text{mg}_3\text{xn}$  ( $x = \text{p, as, sb, bi}$ ), *Mater. Today Phys.* (2024) 101340.
- 100 A. Lavasani, D. Bulmash, S. D. Sarma, Wiedemann-franz law and fermi liquids, *Phys. Rev. B* 99 (8) (2019) 085104.
- 101 J. He, Y. Xia, S. S. Naghavi, V. Ozoliņš, C. Wolverton, Designing chemical analogs to pbte with intrinsic high band degeneracy and low lattice thermal conductivity, *Nat. Commun.* 10 (1) (2019) 719.
- 102 W. Liu, J. Hu, S. Zhang, M. Deng, C.-G. Han, Y. Liu, New trends, strategies and opportunities in thermoelectric materials: a perspective, *Mater. Today Phys.* 1 (2017) 50–60.

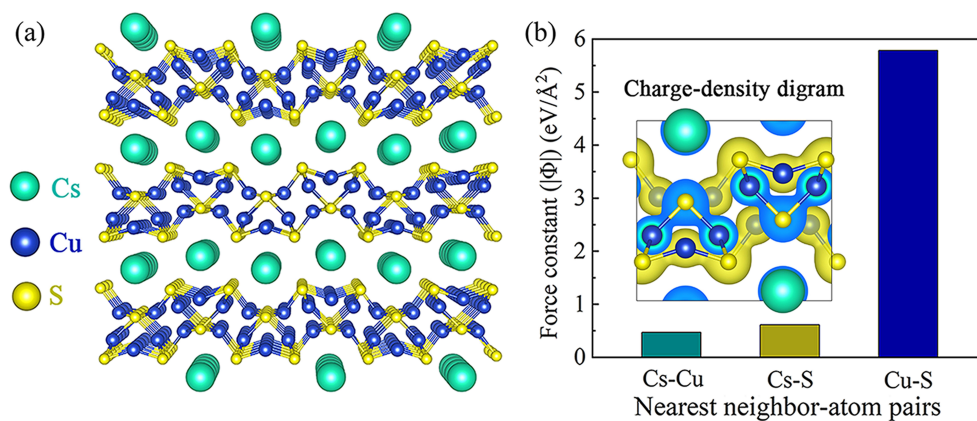


Figure S1: (a) The crystal structure of crystalline *o*-CsCu<sub>5</sub>S<sub>3</sub>, featured by wave-shaped Cu<sub>4</sub>S<sub>4</sub> column units with interspersed Cs atoms. The cyan, blue, and yellow spheres represent cesium, copper, and sulfur atoms, respectively. (b) Calculated second-order interatomic force constants (IFCs) for nearest-neighbor pairs in *o*-CsCu<sub>5</sub>S<sub>3</sub> crystal. The inset of (b) illustrates the total charge-density distribution within the primitive cell of *o*-CsCu<sub>5</sub>S<sub>3</sub>, featuring yellow isosurfaces representing the charge density contours.

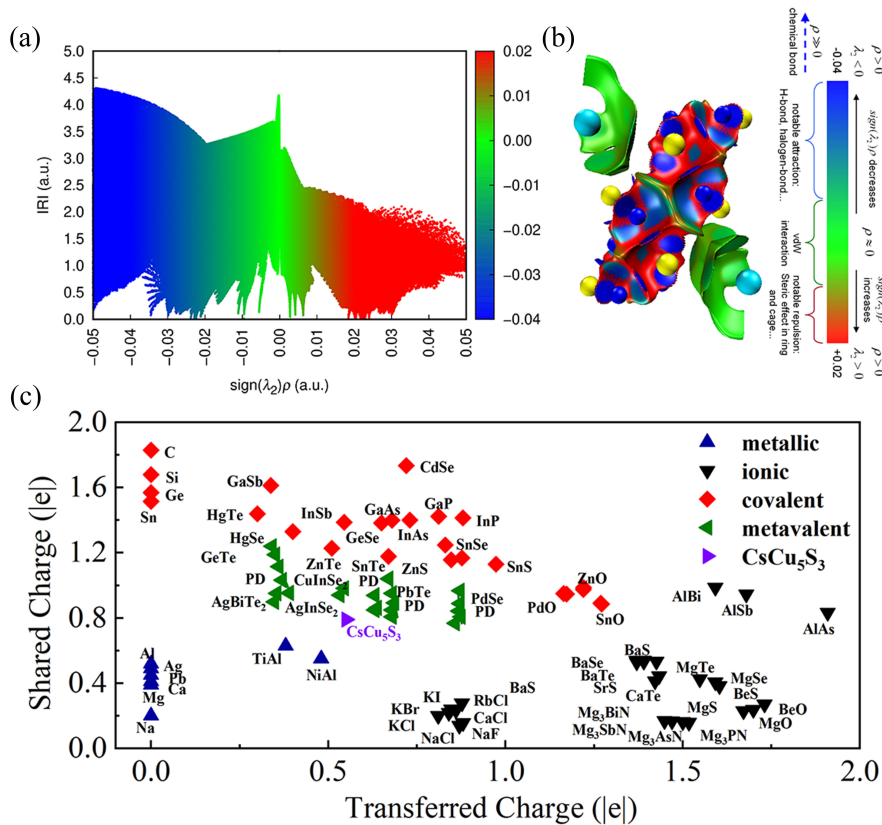


Figure S2: (a) Non-covalent interaction analysis based on interaction region indicator (IRI). Negative and positive  $\text{sign}(\lambda_2)\rho$  denotes attractive and repulsive interactions, respectively, and weak interactions are pervasive in the vicinity of  $\text{sign}(\lambda_2)\rho = 0$ . (b) Isosurface map with standard coloring method and chemical explanation of  $\text{sign}(\lambda_2)\rho$  on IRI isosurfaces. The blue, green, and red areas represent covalent, van der Waals, and repulsive interactions, respectively. (c) Charge sharing and charge transfer map involving metallic, ionic, covalent, and metavalent bonds. The symbols with “PD” indicate the same compounds with Peierl’s distortion. Note that all the data in the figure except for this work are from Ref[66]

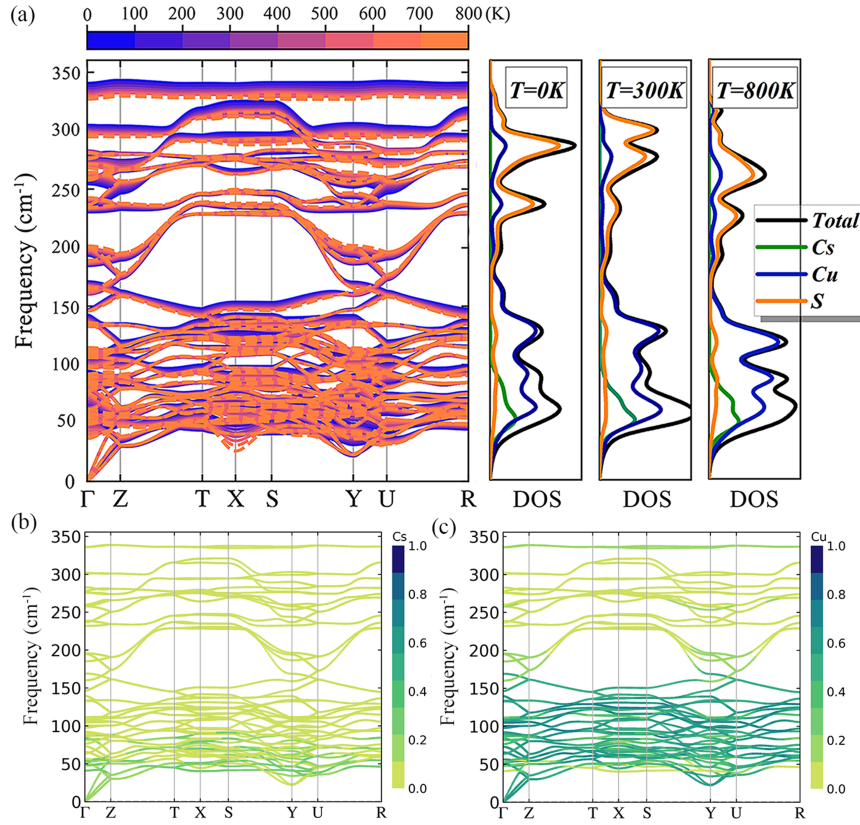


Figure S3: (a) Calculated anharmonically renormalized phonon dispersions at finite temperatures and compared with the zero-K phonon dispersions obtained by using harmonic approximation. The right panel shows the decomposed-atom partial and total phonon densities of states (DOS) at 0 K, 300 K, and 800 K, respectively. (b) The color-coded atomic participation ratio (APR) of Cs atoms projected onto the phonon dispersions at 300 K. (c) The same as (b) but for Cu atoms.

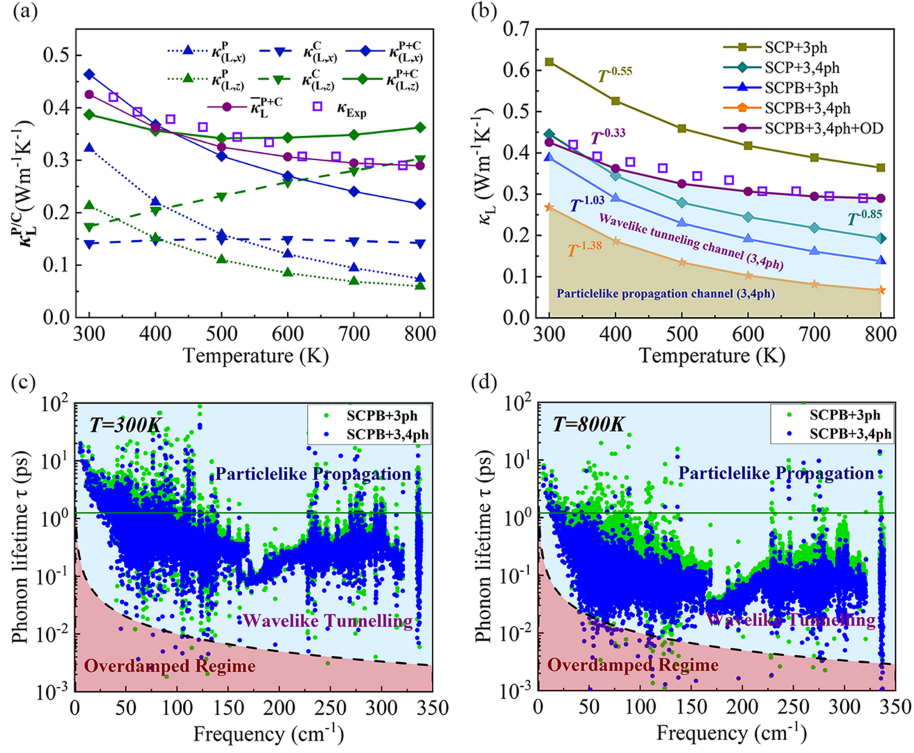


Figure S4: (a) Variations of temperature-dependent thermal conductivity including the contributions from particle-like ( $\kappa_L^P$ ) and wavelike ( $\kappa_L^C$ ) conduction mechanisms by using the SCPB+3,4ph+OD model. (b) Temperature dependence of  $\kappa_L$  based on various theories including the SCP/SCPB + 3/4ph, SCPB + 3,4ph + OD models. The SCPB+3,4ph+OD model reveals that the phonon and coherence channels contribute to thermal transport in the orange and blue regions, respectively. (c) Calculated phonon lifetime as a function of frequency at 300 K, where black dotted line and green solid line represent the Ioffe-Regel limit and Wigner limit in time. (d) The same as (c), but for 800 K.

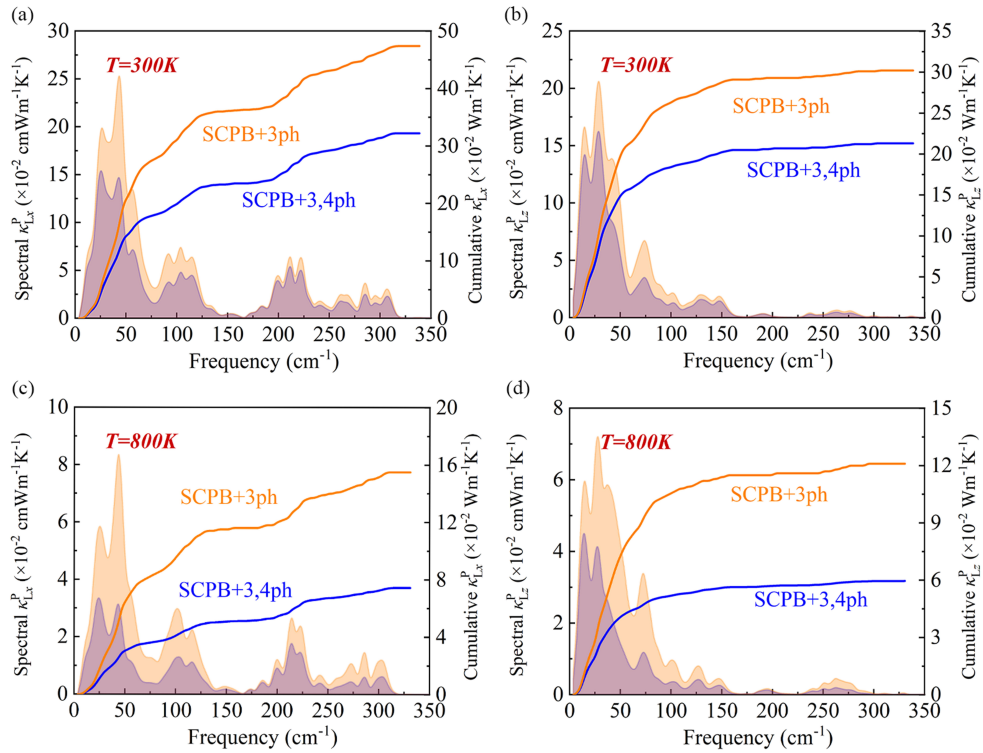


Figure S5: Calculated spectral/cumulative populations' thermal conductivity using the SCPB+3ph and SCPB+3,4ph models, at 300 and 800 K, respectively. (a) Spectral and cumulative populations' thermal conductivity along  $x$  axis at 300 K. (b) The same as (a) but along  $z$  axis. (c) The same as (a) but for 800 K. (d) The same as (b) but for 800 K.



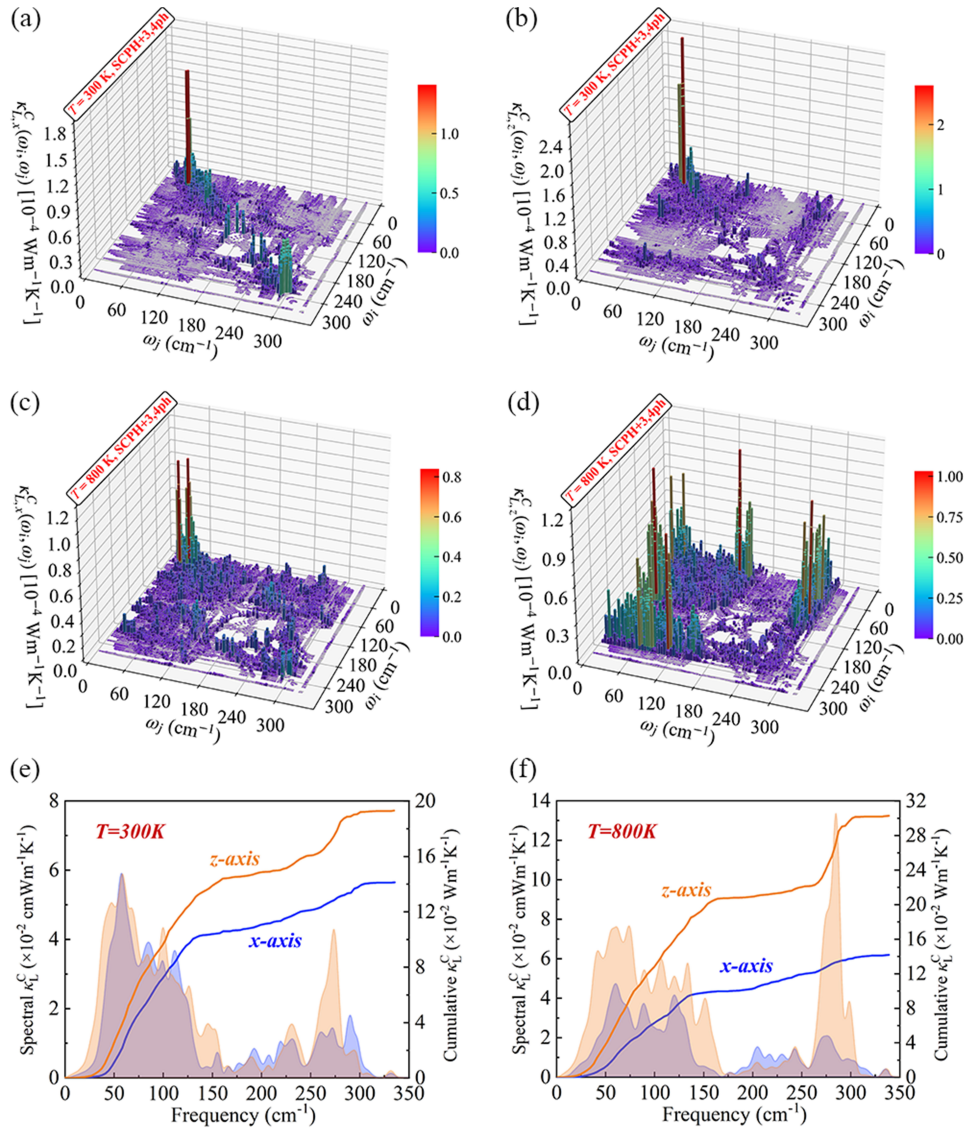


Figure S6: (a) Three-dimensional visualizations modal  $\kappa_L^C(\omega_{qj}, \omega_{qj'})$  of the contributions to the coherences' thermal conductivity calculated by the SCPB+3,4ph+OD model along with the  $x$  axis at 300 K. The diagonal data points ( $\omega_{qj} = \omega_{qj'}$ ) indicate phonon degenerate eigenstates. (b) The same as (a), but for  $z$  axis. (c) The same as (a), but for 800 K. (d) The same as (b), but for 800 K. (e) Spectral and cumulative coherences' thermal conductivity along  $x$  and  $z$  direction at 300 K. (f) The same as (e), but for 800 K.

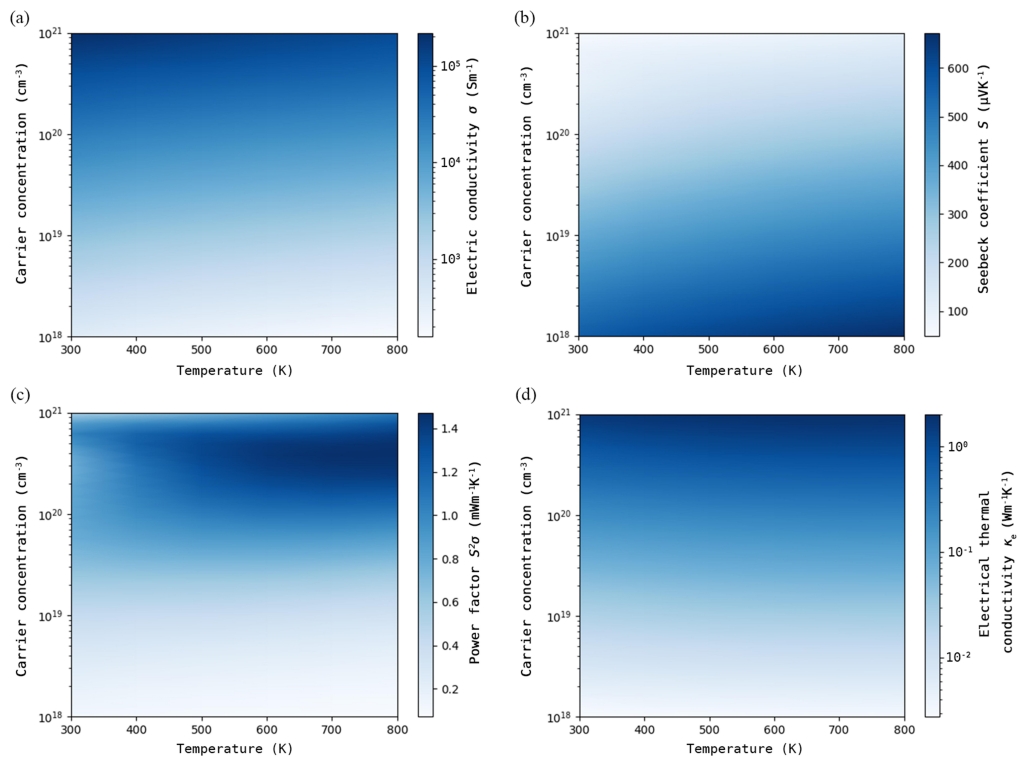


Figure S7: Calculated *p*-type electronic transport properties involving (a) electrical conductivity  $\sigma$ , (b) Seebeck coefficient  $S$ , (c) power factor PF, (d) electrical thermal conductivity  $\kappa_e$ , corresponding to carrier concentrations from  $10^{18} \text{ cm}^{-3}$  to  $10^{21} \text{ cm}^{-3}$  and temperatures from 300 K to 800 K.

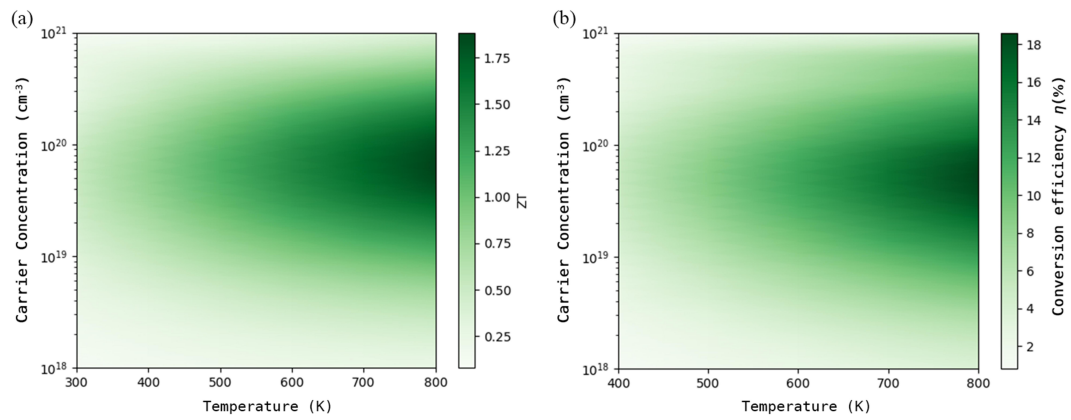


Figure S8: (a) Calculated p-type thermoelectric figure of merit  $ZT$  corresponding to carrier concentrations ranging from  $10^{18} \text{ cm}^{-3}$  to  $10^{21} \text{ cm}^{-3}$  and temperatures spanning from 300 K to 800 K. (b) Theoretically optimal thermoelectric conversion efficiency  $\eta$  (%) corresponding to carrier concentrations from  $10^{18} \text{ cm}^{-3}$  to  $10^{21} \text{ cm}^{-3}$  and hot end temperatures from 400 K to 800 K, where the cold end defaults to 300 K.